Nanoscale Advances

ROYAL SOCIETY OF CHEMISTRY

PAPER

View Article Online
View Journal | View Issue

Check for updates

Cite this: *Nanoscale Adv.*, 2024, **6**, 5106

PtRu mesoporous nanospheres as electrocatalysts with enhanced performance for oxidation of methanol†

Jiangbin Guo, [a] Qiyu Yan,[a] Man Zhang,[b] Jun Fang,[a] Shuiyuan Luo[a] and Jing Xu *[a]

Received 13th March 2024
Accepted 7th August 2024

DOI: 10.1039/d4na00210e

rsc.li/nanoscale-advances

Composition and morphology are crucial factors in the design of Pt-based catalysts with high performance, particularly in direct methanol fuel cells (DMFCs). Herein, PtRu mesoporous nanospheres (PtRu MNs) with tunable compositions were synthesized *via* a facile method and then deposited on a carbon support to act as electrocatalyst materials for the methanol oxidation reaction (MOR). Superior catalytic activity, better catalytic stability, and good tolerance to CO were achieved by the optimum PtRu (2 : 1) MNs/C catalyst compared with Pt MNs/C. The mass activity on PtRu (2 : 1) MNs/C reached 111.77 mA mg_{Pt}^{-1}, which was approximately 6.45-fold higher than that of Pt MNs/C (17.33 mA mg_{Pt}^{-1}). Meanwhile, PtRu (2 : 1) MNs/C retained much more current density (84.7%) than Pt MNs/C (17.7%) after 500 cycles. The improved catalytic performance is due to several factors, including the formation of a mesoporous nanostructure with abundant active sites and the favorable effects of the Ru species. This work provides guidance toward designing and fabricating effective Pt-based electrocatalysts for DMFC applications.

Introduction

The consumption of fossil-based resources and subsequent pollution of the environment have led to growing research interest in sustainable and clean energy resources.[1–5] Fuel cell technology, which directly transforms chemical energy into electrical energy, shows good potential as an alternative power source for a variety of applications.[6–10] Direct methanol fuel cells (DMFCs) are particularly promising because they have excellent energy densities and low emissions. Moreover, methanol fuels are easy to handle.[11–15] The anode in a DMFC is where the methanol oxidation reaction (MOR) happens, and platinum-based materials are the main MOR catalysts. However, the commercialization of DMFCs is hindered by several challenges, such as the scarcity of platinum and its easy CO poisoning, meaning that DMFCs with Pt-based MOR catalysts have high costs and poor fuel cell performance.[16,17] Thus, developing low-cost Pt-based electrocatalysts that exhibit good catalytic properties would be highly significant for the use of DMFCs.

The usage of Pt in MOR electrocatalysts can be reduced by the incorporation of Pt with another metal in an alloy. Moreover, this strategy can dramatically enhance the electrocatalytic performance toward the MOR.[18–22] Among the various bimetallic alloys, PtRu nanocatalysts are regarded as superior DMFC anode catalysts, and the high catalytic activity of these catalysts is explained by the electronic effect and bifunctional mechanism.[23–25] On one hand, Ru species facilitate the dissociative adsorption of H_2O to provide abundant hydroxyl species at lower potentials. This mitigates the CO poisoning of Pt because oxidative CO removal is promoted. On the other hand, the Pt–CO bond strength is reduced by charge transfer from Ru to Pt, which alters the electronic properties of Pt.

Fabricating PtRu nanocatalysts with different morphologies to expose more active sites has been widely investigated to improve their electrocatalytic performance and utilization.[26–30] For example, Huang *et al.*[26] synthesized PtRu nanocubes, nanorods, and nanowires to study the effect of the exposed crystal face on electrocatalytic activity. The PtRu nanowires with {111}-terminated facets showed improved mass activity and better MOR durability than PtRu nanocubes terminated by {100} facets and commercial Pt/C. Dong *et al.*[27] describe a strategy for synthesizing PtRu alloy nanodendrites with tunable compositions. For the electro-oxidation of methanol, the optimum $Pt_{0.8}Ru_{0.2}$ nanodendrite catalyst showed 6.6-fold improved mass activity compared with commercially available Pt/C. Yin and co-workers[28] prepared a special core–shell nanostructured electrocatalyst that contained a bimetallic PtRu mesoporous shell surrounding a Pt core (Pt@mPtRu YSs). This core–shell material exhibited superb electrocatalytic performance, excellent stability, and satisfactory tolerance toward CO as a MOR electrocatalyst because the mesoporous PtRu

[a]*College of Chemical Engineering and Materials, Quanzhou Normal University, Quanzhou, Fujian 362000, P. R. China. E-mail: jingxu@qztc.edu.cn*

[b]*State Key Laboratory of Molecular Engineering of Polymers, Department of Macromolecular Science, Fudan University, Shanghai 200433, P. R. China*

† Electronic supplementary information (ESI) available: Optimization of synthetic conditions and characterization results. See DOI: https://doi.org/10.1039/d4na00210e

nanocage shell and inner Pt nanoparticles had an abundance of active sites.

This study reports a simple approach for the hydrothermal fabrication of PtRu mesoporous nanospheres (PtRu MNs) with tunable compositions *via* $RuCl_3$ and K_2PtCl_4 co-reduction using L-ascorbic acid. The crystal structure, morphology, and surface chemical states of the prepared catalysts were characterized. The optimum PtRu (2 : 1) MNs/C catalyst showed superb catalytic performance and stability for methanol electro-oxidation because its porous nanostructure and Ru species led to a synergistic improvement.

Experimental section

Chemicals and materials

Pluronic F127 (Mn = 13 000), ruthenium chloride ($RuCl_3$, 99%), potassium tetrachloroplatinate (K_2PtCl_4, 98%), L-ascorbic acid (99%), potassium bromide (KBr, AR), ethanol (C_2H_5OH, AR), sulfuric acid (H_2SO_4, 97%), methanol (CH_3OH, AR), and formic acid (HCOOH, AR) were purchased from Sinopharm Chemical Reagent Co., Ltd (China). Vulcan XC-72 carbon black was obtained from Cabot Co. Perfluorinated Nafion ion-exchange resin solution (5 wt%, lower aliphatic alcohol solution with 15–20% water content) was provided by Sigma-Aldrich. No additional chemical purification was performed.

Catalyst preparation

Preparation of PtRu mesoporous nanospheres (PtRu MNs). Aqueous solutions of K_2PtCl_4, $RuCl_3$, and L-ascorbic acid were separately prepared using ultrapure water. Next, 1.5 mL ultrapure water was used to disperse F127 (0.06 g) and KBr (0.2 g). Then, 1.125 mL K_2PtCl_4 solution (0.02 M), 0.5625 mL $RuCl_3$ solution (0.02 M), and 2 mL L-ascorbic acid solution (0.1 M) were added to the mixture of F127 and KBr. This mixed solution was heated for 12 h at 70 °C and then naturally cooled until it reached ambient temperature. A solid was collected by centrifuging the solution (15 min, 10 000 rpm), and this solid was washed with distilled water three times to obtain PtRu MNs.

Preparation of PtRu mesoporous nanospheres supported on Vulcan XC-72 (PtRu MNs/C). The as-synthesized PtRu MNs were uniformly dispersed in 2.5 mL ethanol and 5 mL ultrapure water. Vulcan XC-72 (0.0175 g) was separately dispersed in an ethanol/water solution (1 : 2 v/v ratio of ethanol/water, 15 mL) *via* sonication for 30 min. Next, the PtRu MNs and Vulcan XC-72 suspensions were combined and homogeneously mixed by sonicating for an additional 1 h. This mixture was centrifuged to obtain PtRu MNs/C, which was then washed with distilled water three times. Finally, the product was dried for 24 h under vacuum at 60 °C.

Preparation of Pt mesoporous nanospheres supported on Vulcan XC-72 (Pt MNs/C). As the reference catalyst, Pt MNs/C was also fabricated using a similar procedure as described above. 0.06 g of F127 and 0.2 g of KBr were dispersed in 1.5 mL ultrapure water and then 1.125 mL of K_2PtCl_4 (20 mM) and 2 mL of L-ascorbic acid (0.1 M) were added into the mixture, followed by heating at 70 °C for 12 h. After collecting and washing the product, Pt MNs were uniformly deposited on Vulcan XC-72 to obtain Pt MNs/C.

Characterization of electrocatalysts

A Rigaku RINT Ultima X-ray diffractometer (XRD) was operated with Cu Kα X-rays (λ = 1.5418 Å) to study the crystallographic information. The spectra were acquired over the angular 2θ range 20–80° with a scanning rate of 10° min^{-1}. A Phenom Pharos scanning electron microscope (SEM) was used to evaluate morphology. The samples were placed in the specimen holder, and scrutinized using a scanning electron detector at an accelerated voltage of 15 kV. An FEI Talos F200x G2 transmission electron microscope (TEM, 200 kV) was utilized to obtain TEM micrographs, high-angle annular dark-field scanning TEM (HAADF-STEM) micrographs, and elemental mappings. The samples were dispersed in ethanol, and small droplets of suspensions were placed on carbon-coated copper grids for observation. A PHI 5000 Versaprobe III X-ray photoelectron spectrometer (XPS) was operated with monochrome Al Kα radiation (1486.7 eV), and the analysis chamber was maintained at about 2×10^{-10} mbar. All of the binding energies were calibrated relative to the standard C 1s peak at 284.6 eV.

Electrochemical testing

The working electrode had a 0.196 cm^2 surface area and was prepared with a modified glassy carbon electrode (GCE), the counter electrode was a pure Pt wire, and the reference electrode was Ag/AgCl (saturated KCl). A Metrohm Autolab PGSTAT302N electrochemical analyzer was employed for measurements with a 3-electrode cell. Working electrodes were fabricated by thoroughly combining 2 mg of catalyst with 4.6 μL Nafion, 164 μL ethanol, and 164 μL distilled water. To prepare a homogeneously mixed ink, this mixture was ultrasonicated for 20 min. After that, 6 μL catalyst ink was used to coat the GCE, which was naturally dried under ambient conditions. Cyclic voltammetry (CV) curves were obtained in methanol or formic acid aqueous solutions. The methanol oxidation reaction (MOR) was performed in a solution containing 0.5 M CH_3OH and 0.5 M H_2SO_4 within the potential range of 0–1.2 V at a 50 mV s^{-1} scan rate. Long-term catalytic stability was evaluated for 500 cycles under the same conditions. Chronoamperometry (CA) was performed for 3600 s in a solution containing 0.5 M CH_3OH and 0.5 M H_2SO_4 at a potential of 0.85 V. Electrochemical impedance spectroscopy (EIS) was performed at the frequency range from 100 kHz to 0.1 Hz in 0.5 M CH_3OH with 0.5 M H_2SO_4. CO stripping voltammetry was performed in 0.5 M H_2SO_4 electrolyte. CO was purged into the H_2SO_4 solution for fully adsorbing on the catalyst at 0 V, and the excess CO was purged out by N_2. Electrocatalytic performance and long-term stability of the as-prepared nanocatalysts toward the formic acid oxidation reaction (FAOR) were studied in a solution containing 0.5 M HCOOH and 0.5 M H_2SO_4. Potentials were converted to values with respect to a reversible hydrogen electrode (RHE).

Results and discussion

Synthesis

The PtRu MNs were prepared using a simple one-pot synthesis procedure with K_2PtCl_4 and $RuCl_3$ as the metal precursors. These precursors were reduced using L-ascorbic acid, and the surfactant Pluronic F127 was employed as a structure-directing agent to provide porosity in the PtRu MNs. To study the effect of KBr in this synthesis, the use of KCl was also investigated in a control experiment. As shown in Fig. S1 (ESI),† almost no PtRu MNs are generated when KCl is used instead of KBr, indicating that the metal precursors are not reduced by L-ascorbic acid. This likely indicates that KBr causes the generation of $[PtBr_4]^{2-}$ species with a lower redox potential (0.58 V) *via* ligand exchange between $[PtCl_4]^{2-}$ and Br^-, resulting in the co-reduction of the metal precursors to obtain PtRu MNs.[31] By varying the amount of $RuCl_3$, mesoporous nanospheres with different Pt/Ru ratios were fabricated (Table S1, ESI†). Each prepared PtRu MNs catalyst was deposited on a carbon support for further characterization and evaluation in the methanol oxidation reaction. For comparison, Pt MNs/C was also prepared using the same method.

Morphology

SEM images of all PtRu MNs/C samples and Pt MNs/C are displayed in Fig. S2 (ESI),† revealing that the carbon support contains a uniform dispersion of the obtained mesoporous nanospheres. SEM and TEM images of a typical PtRu MNs sample show many surface protrusions, which indicate the formation of a mesoporous nanostructure (Fig. 1). The spherical bimetallic PtRu nanoparticles have diameters of approximately 180 nm. In addition, the composition of PtRu MNs was evaluated by studying the distribution of elements. The nanospheres contain a homogeneous distribution of the two metals, demonstrating the likely creation of a PtRu alloy (Fig. 2).

Crystallography

PtRu MNs/C and Pt MNs/C were investigated by XRD, as depicted in Fig. 3. A peak at 28° is ascribed to the C (002) crystal plane of the carbon support. The presence of face-centered cubic (fcc) Pt is indicated by the diffraction peaks located at about 39°, 46°, and 67°, which correspond to the (111), (200), and (220) crystal facets, respectively. Compared with Pt MNs/C, the incorporation of Ru causes these peaks to slightly shift toward higher 2θ values. This indicates the generation of a PtRu bimetallic alloy *via* Ru atom incorporation into the Pt lattice.[32] Moreover, no phase separation and the successful formation of the alloy nanostructure are also demonstrated by the absence of diffraction peaks originating from Ru and Ru oxides.

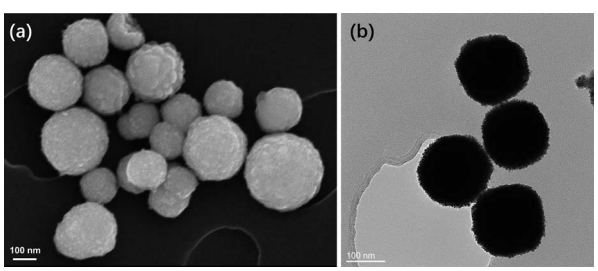

Fig. 1 Representative (a) SEM and (b) TEM micrographs of typical PtRu MNs.

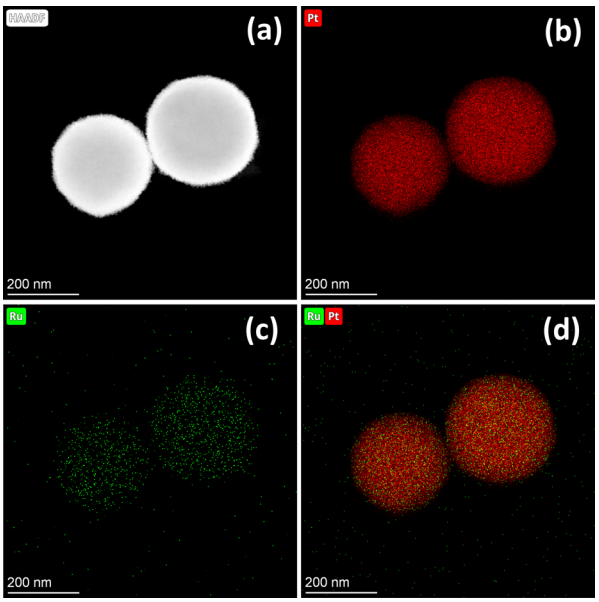

Fig. 2 (a) HAADF-STEM micrograph and elemental distributions of (b) Pt and (c) Ru, and (d) their overlap in PtRu MNs.

Surface chemical states

The electronic properties of PtRu MNs/C were explored by XPS. The Pt 4f region (Fig. 4a) displays a pair of deconvoluted Pt $4f_{7/2}$ and Pt $4f_{5/2}$ doublets, and the strong signals at 71.67 and 74.98 eV are ascribed to Pt metal. No peaks related to PtO, $Pt(OH)_2$, or other Pt(II) species can be observed. The Ru 3d spectrum (Fig. 4b) shows Ru $3d_{5/2}$ and Ru $3d_{3/2}$ signals at 283.36 and 287.34 eV attributed to Ru(VI). Compared with pure Pt, the

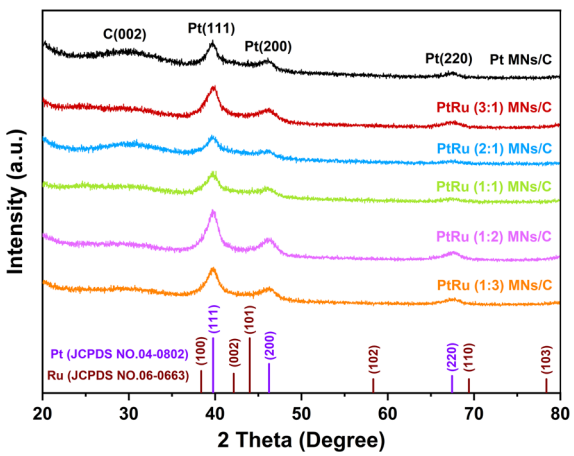

Fig. 3 XRD patterns of PtRu MNs/C and Pt MNs/C.

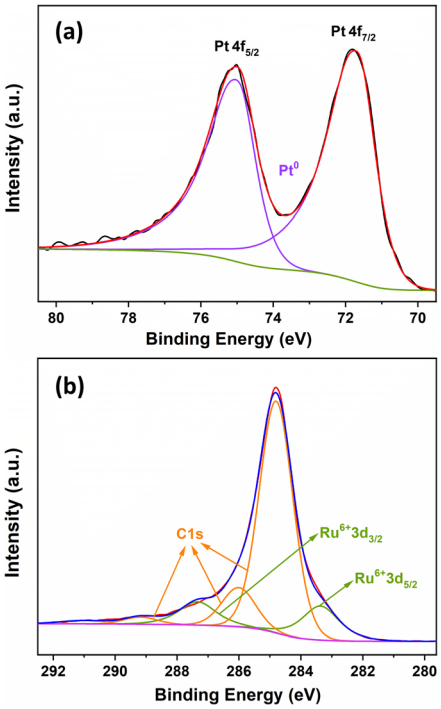

Fig. 4 XPS analysis of PtRu MNs/C for (a) Pt 4f and (b) Ru 3d.

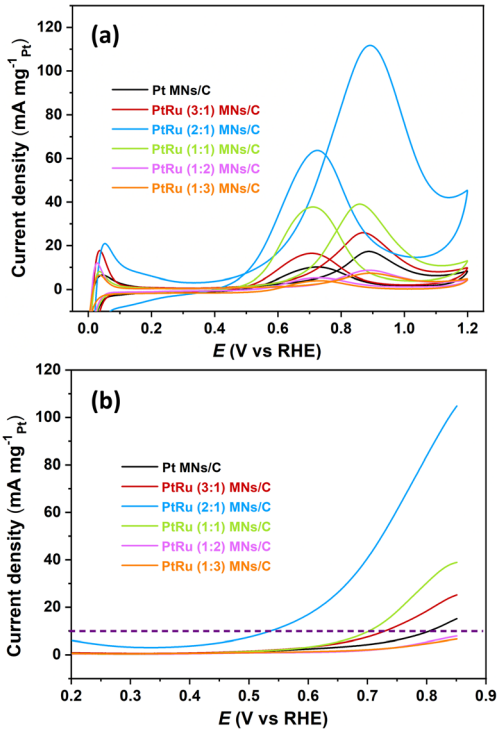

Fig. 5 (a) Cyclic voltammetry profiles of PtRu MNs/C and Pt MNs/C for the MOR. (b) Magnified view of CV curves between 0.2 and 0.85 V.

Pt 4f peaks of PtRu MNs/C show a slight peak shift, demonstrating that Pt may electronically interact with Ru.[28] Ru is known to have a stronger affinity for oxygen than Pt.[19] Therefore, the presence of Ru species in PtRu MNs/C prevents the oxidation of Pt. Moreover, the presence of Ru oxide species provides the catalyst with better electron-proton conductivity and facilitates the generation of Ru–OH species, resulting in much better catalytic performance.[33]

Electrocatalytic activity and durability

Cyclic voltammetry (CV) was performed to evaluate PtRu MNs/C and Pt MNs/C electrocatalyst performance toward the MOR. Two irreversible oxidation peaks are observable in each CV curve (Fig. 5a). The oxidation of methanol on the Pt surface is responsible for the forward peak, while the reverse peak can potentially be attributed to either carbonaceous intermediate species oxidation or the MOR on regenerated Pt active sites after removing residual species.[34,35] Electrocatalytic performance was evaluated by the forward peak current density and the ratio of I_f (forward scan peak current) to I_b (reverse scan peak current), as summarized in Table S2 (ESI).† Among the prepared PtRu-based catalysts, PtRu (2 : 1) MNs/C shows the best mass activity (111.77 mA mg_{Pt}^{-1}). In contrast, the corresponding activity of Pt MNs/C (17.33 mA mg_{Pt}^{-1}) is about 6.45 times lower than that of PtRu (2 : 1) MNs/C. Moreover, PtRu (2 : 1) MNs/C shows significantly lower methanol oxidation potentials than the other nanocatalysts. Specifically, the oxidation potential of PtRu (2 : 1) MNs/C is negatively shifted by *ca.* 0.26 V compared with Pt MNs/C at 10 mA mg_{Pt}^{-1} (dotted line in Fig. 5b). Electrochemical impedance spectroscopy (EIS) was performed to assess the charge transfer resistance of methanol oxidation for different catalysts (Fig. S3, ESI†). It is obvious that the main arc diameter of PtRu (2 : 1) MNs/C is smaller than that of Pt MNs/C, suggesting a faster charge transfer capacity toward the MOR.[36,37] Besides that, PtRu (2 : 1) MNs/C also shows a larger I_f/I_b ratio (1.75) than the other prepared catalysts. A higher I_f/I_b ratio indicates that fewer residual carbonaceous species are accumulated on the Pt surface.[38,39] Therefore, PtRu (2 : 1) MNs/C is more resistant to being poisoned by intermediates compared to the other catalysts. Moreover, the comparison of mass activities between PtRu (2 : 1) MNs/C and commercial Pt/C is illustrated in Fig. S4 (ESI).† It can be seen that the commercial one exhibits higher current density (208.86 mA mg_{Pt}^{-1}) with a lower I_f/I_b ratio (0.91) than the as-prepared PtRu (2 : 1) MNs/C.

The successful application of electrocatalysts in the MOR requires good long-term stability and durability. Therefore, CV curves of PtRu (2 : 1) MNs/C and Pt MNs/C were also obtained over 500 consecutive cycles. Long-term stability was estimated by comparing the I_f values of the initial cycle and the 500th cycle, as shown in Fig. 6a and b. PtRu (2 : 1) MNs/C retains 84.7% of its first-cycle I_f value after 500 cycles, while Pt MNs/C only retains 17.7% (Fig. 6c). Next, chronoamperometry (CA) measurements were performed to investigate the constant-potential durability of the catalysts (Fig. 6d). In the first few seconds, all catalysts show a rapid decline in MOR current density because intermediate carbonaceous species cause the active sites to be poisoned.[40] However, PtRu (2 : 1) MNs/C exhibits an enhanced current density compared to Pt MNs/C across the entire testing period. To deeply investigate the CO

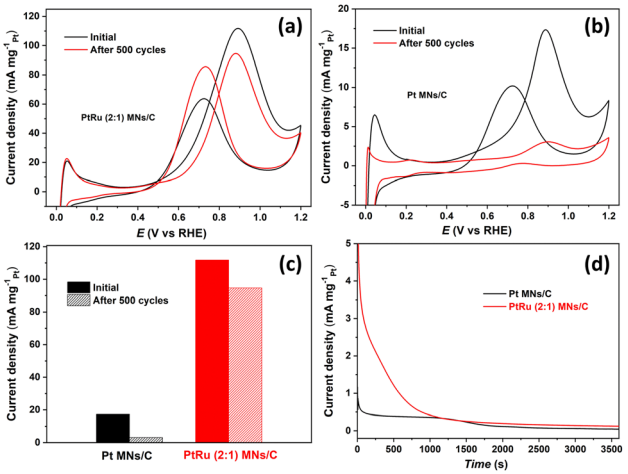

Fig. 6 CV curves of (a) PtRu (2 : 1) MNs/C and (b) Pt MNs/C before and after 500 potential cycles for the MOR. (c) Loss of mass activity of different electrocatalysts. (d) Chronoamperometry curves of PtRu (2 : 1) MNs/C and Pt MNs/C for the MOR.

tolerance of catalysts, CO stripping voltammograms were recorded in 0.5 M H_2SO_4 at a sweep rate of 20 mV s^{-1}, as shown in Fig. S5 (ESI).† It is observed that PtRu (2 : 1) MNs/C and Pt MNs/C show a sharp peak in the first positive scan, which is due to oxidation of the adsorbed CO on the surface of the electrocatalyst. However, the CO oxidation peak of PtRu (2 : 1) MNs/C at 0.63 V is much more negative than that of Pt MNs/C (0.77 V), indicating a critical role of Ru species in enhancing the CO tolerance ability of the catalyst.[41,42] These results clearly demonstrate that PtRu (2 : 1) MNs/C has excellent MOR activity and good catalytic stability/durability.

Another potential liquid fuel that can be used in fuel cells is formic acid. Platinum electrocatalysts have also been widely employed in the formic acid oxidation reaction (FAOR).[43–45] To evaluate the applicability of PtRu MNs/C in the FAOR, CV curves of all as-synthesized samples were obtained. The forward scan has two oxidation peaks based on the reaction mechanism. The peak at ~0.6 V (I_{f_1}) is due to the direct pathway (direct formation of CO_2), while that at ~1.0 V (I_{f_2}) is related to the indirect pathway (CO formed as an intermediate poison).[46] As illustrated in Fig. S6 (ESI),† all the obtained CV curves show a higher I_{f_2} current density and negligible I_{f_1} current density. This suggests that the Ru in PtRu MNs/C does not promote the direct pathway, which can be ascribed to the presence of two oxygens in HCOOH.[47] However, the I_{f_2} mass activity of PtRu (2 : 1) MNs/C is 218.90 mA mg_{Pt}^{-1}, which exceeds those of the other PtRu MNs/C catalysts and is about 13.14 times higher than that of Pt MNs/C (16.66 mA mg_{Pt}^{-1}). Electrocatalyst stability in the FAOR was tested by obtaining CV curves across 500 consecutive cycles (Fig. S7a and b, ESI†). The mass activity losses are summarized in Fig. S7c (ESI),† and the PtRu (2 : 1) MNs/C electrocatalyst shows a decline of 22.6% compared with its initial catalytic activity, while Pt MNs/C retains 79.9% of its initial activity.

The excellent electrocatalytic activity of PtRu (2 : 1) MNs/C can be attributed to two main reasons: (1) the mesoporosity of the PtRu (2 : 1) MNs/C structure provides an abundance of accessible active sites, leading to improved MOR activity; (2) the presence of the Ru element in PtRu MNs provides abundant oxygen-containing species during the MOR, which enhances catalyst durability by increasing the resistance to CO_{ads} poisoning.

Conclusions

In summary, a series of electrocatalysts consisting of well-dispersed bimetallic PtRu MNs on carbon were successfully synthesized and employed as MOR catalysts. SEM and TEM images confirmed the presence of a mesoporous nanostructure, which effectively provided abundant active sites. XPS analysis indicated the existence of metallic Pt and oxidized Ru, which facilitated the removal of intermediate poisons adsorbed on the Pt surface. Benefiting from its nanostructure and composition, the optimum PtRu (2 : 1) MNs/C catalyst exhibited superb MOR catalytic activity. Electrochemical analysis showed that PtRu (2 : 1) MNs/C had a much larger current density compared to Pt MNs/C. Moreover, the larger I_f/I_b ratio of PtRu (2 : 1) MNs/C revealed that this catalyst had a stronger ability to resist the accumulation of carbonaceous substances. PtRu (2 : 1) MNs/C was also more durable (lower decline in mass activity and current density) than the other prepared catalysts, as demonstrated by CV curves and chronoamperometry. The results and analysis reported herein offer a compelling strategy for designing efficient Pt-based anode electrocatalysts for the MOR in DMFCs.

Data availability

The data supporting this article have been included as part of the ESI.†

Author contributions

Jiangbin Guo: conceptualization, investigation, formal analysis, data curation, visualization, writing – original draft, writing – review & editing. Qiyu Yan: investigation, formal analysis, data curation. Man Zhang: investigation, formal analysis. Jun Fang: conceptualization, writing – review & editing, funding acquisition. Shuiyuan Luo: writing – review & editing, funding acquisition. Jing Xu: conceptualization, methodology, formal analysis, supervision, funding acquisition, writing – original draft, writing – review & editing.

Conflicts of interest

There are no conflicts to declare.

Acknowledgements

This work was supported by the Natural Science Foundation of Fujian Province (grant no. 2022J011100 and 2020J05155), the National Natural Science Foundation of China (grant no. 21676222 and U1705252), the Science and Technology Major

Special Project of Fujian Province (grant no. 2020HZ06019), the Quanzhou City Science and Technology Program of China (grant no. 2019C106), and the Scientific Research Foundation of Quanzhou Normal University (grant no. H18001 and H17015).

References

1 J. Li, L. Zhao, X. Li, S. Hao and Z. Wang, *J. Energy Chem.*, 2020, **40**, 7–14.
2 B. Wu, C. Wu, J. Zhu, X. Li, J. Chu, X. Wang and S. Xiong, *Ionics*, 2020, **26**, 4599–4608.
3 Y. V. Tolmachev and O. A. Petrii, *J. Solid State Electrochem.*, 2017, **21**, 613–639.
4 K. M. Yeo, S. Choi, R. M. Anisur, J. Kim and I. S. Lee, *Angew. Chem., Int. Ed.*, 2011, **50**, 745–748.
5 X. Liu, K. Wang, L. Zhou, H. Pu, T. Zhang, J. Jia and Y. Deng, *ACS Sustainable Chem. Eng.*, 2020, **8**, 6449–6457.
6 G. Montiel, E. Fuentes-Quezada, M. M. Bruno, H. R. Corti and F. A. Viva, *RSC Adv.*, 2020, **10**, 30631–30639.
7 D. L. Quan and P. H. Le, *Coatings*, 2021, **11**, 571.
8 J. Zhang, S. Lu, Y. Xiang and S. P. Jiang, *ChemSusChem*, 2020, **13**, 2484–2502.
9 I. Staffell, D. Scamman, A. Velazquez Abad, P. Balcombe, P. E. Dodds, P. Ekins, N. Shah and K. R. Ward, *Energy Environ. Sci.*, 2019, **12**, 463–491.
10 L. van Biert, M. Godjevac, K. Visser and P. V. Aravind, *J. Power Sources*, 2016, **327**, 345–364.
11 B. G. Abraham, R. Bhaskaran and R. Chetty, *J. Electrochem. Soc.*, 2020, **167**, 024512.
12 Y. Feng, H. Liu and J. Yang, *Sci. Adv.*, 2017, **3**, e1700580.
13 A. S. Moura, J. L. C. Fajín, M. Mandado and M. N. D. S. Cordeiro, *Catalysts*, 2017, **7**, 47.
14 Y. Zhao, J. Liu, C. Liu, F. Wang and Y. Song, *ACS Catal.*, 2016, **6**, 4127–4134.
15 Y. Wang, M. Zheng, H. Sun, X. Zhang, C. Luan, Y. Li, L. Zhao, H. Zhao, X. Dai, J.-Y. Ye, H. Wang and S.-G. Sun, *Appl. Catal., B*, 2019, **253**, 11–20.
16 L. Bai, *J. Sol–Gel Sci. Technol.*, 2022, **103**, 118–124.
17 A. Garg, M. Milina, M. Ball, D. Zanchet, S. T. Hunt, J. A. Dumesic and Y. Román-Leshkov, *Angew. Chem., Int. Ed.*, 2017, **56**, 8828–8833.
18 A. Kaur, G. Kaur, P. P. Singh and S. Kaushal, *Int. J. Hydrogen Energy*, 2021, **46**, 15820–15849.
19 J. Guo, M. Zhang, J. Xu, J. Fang, S. Luo and C. Yang, *RSC Adv.*, 2022, **12**, 2246–2252.
20 E. Taylor, S. Chen, J. Tao, L. Wu, Y. Zhu and J. Chen, *ChemSusChem*, 2013, **6**, 1863–1867.
21 Z. Qi, C. Xiao, C. Liu, T. W. Goh, L. Zhou, R. Maligal-Ganesh, Y. Pei, X. Li, L. A. Curtiss and W. Huang, *J. Am. Chem. Soc.*, 2017, **139**, 4762–4768.
22 Y. Lu, Y. Jiang and W. Chen, *Nanoscale*, 2014, **6**, 3309–3315.
23 M. Wakisaka, S. Mitsui, Y. Hirose, K. Kawashima, H. Uchida and M. Watanabe, *J. Phys. Chem. B*, 2006, **110**, 23489–23496.
24 S. Lu, K. Eid, D. Ge, J. Guo, L. Wang, H. Wang and H. Gu, *Nanoscale*, 2017, **9**, 1033–1039.
25 Q. Wang, Y.-W. Zhou, Z. Jin, C. Chen, H. Li and W.-B. Cai, *Catalysts*, 2021, **11**, 925.
26 L. Huang, X. Zhang, Q. Wang, Y. Han, Y. Fang and S. Dong, *J. Am. Chem. Soc.*, 2018, **140**, 1142–1147.
27 K. Dong, H. Pu, T. Zhang, H. Dai, X. Zhao, L. Zhou, K. Wang, Y. Wang and Y. Deng, *J. Alloys Compd.*, 2022, **905**, 164231.
28 S. Yin, R. D. Kumar, H. Yu, C. Li, Z. Wang, Y. Xu, X. Li, L. Wang and H. Wang, *ACS Sustainable Chem. Eng.*, 2019, **7**, 14867–14873.
29 H. Xu, H. Shang, C. Wang and Y. Du, *Adv. Funct. Mater.*, 2020, **30**, 2000793.
30 H. Tian, Y. Yu, Q. Wang, J. Li, P. Rao, R. Li, Y. Du, C. Jia, J. Luo, P. Deng, Y. Shen and X. Tian, *Int. J. Hydrogen Energy*, 2021, **46**, 31202–31215.
31 H. Wang, H. Yu, S. Yin, Y. Li, H. Xue, X. Li, Y. Xu and L. Wang, *Nanoscale*, 2018, **10**, 16087–16093.
32 G. Garcia, V. Baglio, A. Stassi, E. Pastor, V. Antonucci and A. S. Aricò, *J. Solid State Electrochem.*, 2007, **11**, 1229–1238.
33 L. Bai, *Appl. Surf. Sci.*, 2018, **433**, 279–284.
34 A. Elangovan, J. Xu, A. Sekar, B. Liu and J. Li, *ChemCatChem*, 2020, **12**, 6000–6012.
35 A. Sekar, N. Metzger, S. Rajendran, A. Elangovan, Y. Cao, F. Peng, X. Li and J. Li, *ACS Appl. Nano Mater.*, 2022, **5**, 3275–3288.
36 W. Qiao, L. Yu, J. Chang, F. Yang and L. Feng, *Chin. J. Catal.*, 2023, **51**, 113–123.
37 M. Li, F. Yang, J. Chang, A. Schechter and L. Feng, *Acta Phys.-Chim. Sin.*, 2023, **39**, 2301005.
38 Y. Shi, W. Zhu, H. Shi, F. Liao, Z. Fan and M. Shao, *J. Colloid Interface Sci.*, 2019, **557**, 729–736.
39 Y. Sang, R. Zhang, B. Xu, J. Yang, C. Zhao and H. Xu, *ACS Appl. Energy Mater.*, 2022, **5**, 4179–4190.
40 J. Zhang, X. Qu, Y. Han, L. Shen, S. Yin, G. Li, Y. Jiang and S. Sun, *Appl. Catal., B*, 2020, **263**, 118345.
41 X. Ding, M. Li, J. Jin, X. Huang, X. Wu and L. Feng, *Chin. Chem. Lett.*, 2022, **33**, 2687–2691.
42 C. Liu and L. Feng, *Chin. J. Struct. Chem.*, 2023, **42**, 100136.
43 X. Yu and P. G. Pickup, *J. Power Sources*, 2008, **182**, 124–132.
44 T. Chen, C. Ge, Y. Zhang, Q. Zhao, F. Hao and N. Bao, *Int. J. Hydrogen Energy*, 2015, **40**, 4548–4557.
45 J. Xu, M. Zhao, S.-i. Yamaura, T. Jin and N. Asao, *J. Appl. Electrochem.*, 2016, **46**, 1109–1118.
46 K. Jiang, H.-X. Zhang, S. Zou and W.-B. Cai, *Phys. Chem. Chem. Phys.*, 2014, **16**, 20360–20376.
47 M. S. Çögenli and A. B. Yurtcan, *Int. J. Hydrogen Energy*, 2018, **43**, 10698–10709.